ANL/NE-15/32

V&V of CFD Modeling of the Argonne Bubble Experiment FY15 Summary Report

Nuclear Engineering Division

About Argonne National Laboratory
Argonne is a U.S. Department of Energy laboratory managed by UChicago Argonne, LLC under contract DE-AC02-06CH11357. The Laboratory's main facility is outside Chicago, at 9700 South Cass Avenue, Argonne, Illinois 60439. For information about Argonne and its pioneering science and technology programs, see www.anl.gov.

DOCUMENT AVAILABILITY

Online Access: U.S. Department of Energy (DOE) reports produced after 1991 and a growing number of pre-1991 documents are available free via DOE's SciTech Connect (http://www.osti.gov/scitech/).

Reports not in digital format may be purchased by the public from the National Technical Information Service (NTIS):
U.S. Department of Commerce
National Technical Information Service
5301 Shawnee Rd
Alexandria, VA 22312
www.ntis.gov
Phone: (800) 553-NTIS (6847) or (703) 605-6000
Fax: (703) 605-6900
Email: **orders@ntis.gov**

Reports not in digital format are available to DOE and DOE contractors from the Office of Scientific and Technical Information (OSTI):
U.S. Department of Energy
Office of Scientific and Technical Information
P.O. Box 62
Oak Ridge, TN 37831-0062
www.osti.gov
Phone: (865) 576-8401
Fax: (865) 576-5728
Email: **reports@osti.gov**

Disclaimer
This report was prepared as an account of work sponsored by an agency of the United States Government. Neither the United States Government nor any agency thereof, nor UChicago Argonne, LLC, nor any of their employees or officers, makes any warranty, express or implied, or assumes any legal liability or responsibility for the accuracy, completeness, or usefulness of any information, apparatus, product, or process disclosed, or represents that its use would not infringe privately owned rights. Reference herein to any specific commercial product, process, or service by trade name, trademark, manufacturer, or otherwise, does not necessarily constitute or imply its endorsement, recommendation, or favoring by the United States Government or any agency thereof. The views and opinions of document authors expressed herein do not necessarily state or reflect those of the United States Government or any agency thereof, Argonne National Laboratory, or UChicago Argonne, LLC.

ANL/NE-15/32

V&V of CFD Modeling of the Argonne Bubble Experiment FY15 Summary Report

by
Nathaniel Hoyt, Kent E. Wardle and Jim Bailey
Nuclear Engineering Division, Argonne National Laboratory

Manjunath Basavarajappa
University of Utah

September 30, 2015

CONTENTS

1 The Experimental Setup 5

2 CFD Methodology 8

3 CFD Results 11

3.1 Effect of Bubbles 12
3.2 Comparison to Thermocouple Measurements 15
3.3 Comparison to Velocity Measurements 18
3.4 Effect of Central Cooling Channel 19

4 Conclusion 20

5 Acknowledgments 21

6 References 22

Appendix A.1: Thermophysical Properties of Uranyl Sulfate Solution 22

Appendix A.2: CFD Calculations of Thermocouple Internal Heating 23

FIGURES

1 Major Elements of the Bubble-Experiment Apparatus 6

2 Schematic of the Bubble-Experiment Apparatus—Details of Irradiation Vessel 6

3 Photograph of the Assembled Bubble-Experiment Vessel 7

4 Bubble Chamber Geometry and Surface Mesh 9

5 Detailed View of Surface Mesh on Top Surface for Fine Mesh 9

6 Volumetric Power Deposition Field from Incident Radiation and Liquid Free Surface 10

7 Positions of Radiolytically Generated Bubbles in the Uranyl Sulfate Solution 11

8 (a) Time-Averaged Upward Velocity Contours with Indicated Liquid Level; (b) Instantaneous Upward Velocity Contours with Indicated Liquid Level 13

9 (a) Instantaneous Temperature Field; (b) Instantaneous Velocity Vectors Colored by Velocity Magnitude. 14

10 Upward Velocity Profile across the Indicated Line with and without Bubble Generation 15

11 Cross Section of the Experimental Primary Containment Vessel. 16

12 Area-Weighted Average Steady-State Temperature for a Given Depth from Experiments and from Numerical Simulations 17

13 High-Speed Imaging Locations Used for Determination of Bubble Velocities 18

A.2.1. CFD Results for Internal Heating of the Thermocouples 30

TABLES

1 Depth of Thermocouple Channels beneath the Liquid Surface for 20 L Fill Level 16

2 Predicted and Experimentally Estimated Bubble Velocities 19

V&V OF CFD MODELING OF THE ARGONNE BUBBLE EXPERIMENT FY15 SUMMARY REPORT

In support of the development of accelerator-driven production of the fission product Mo-99, computational fluid dynamics (CFD) simulations of an electron-beam irradiated, experimental-scale bubble chamber have been conducted in order to aid in interpretation of existing experimental results, provide additional insights into the physical phenomena, and develop predictive thermal hydraulic capabilities that can be applied to full-scale target solution vessels. Toward that end, a custom hybrid Eulerian-Eulerian-Lagrangian multiphase solver was developed, and simulations have been performed on high-resolution meshes. Good agreement between experiments and simulations has been achieved, especially with respect to the prediction of the maximum temperature of the uranyl sulfate solution in the experimental vessel. These positive results suggest that the simulation methodology that has been developed will prove to be suitable to assist in the development of full-scale production hardware.

1 THE EXPERIMENTAL SETUP

As part of the investigation of the physical phenomena that govern the accelerator-driven production of the fission product Mo-99, a 35 MeV electron linac was used to irradiate a 20 L target solution composed of a depleted-uranium uranyl sulfate sample dissolved in pH 1 sulfuric acid at incident powers of 6 kW, 12 kW, and 15 kW. During this operation, the solution experiences self-heating because of fissioning in the solution, radiolytic decomposition of the water in the solution, and induced circulation due to thermal gradients. As the formation and subsequent dynamic motion of the radiolytically generated bubbles (H_2 and O_2) impact the operational parameters of the liquid target, an understanding of bubble behavior is critical for the ability to predict the behavior of the target solution during this operation. It is also important to be able to predict the thermal gradients and the circulation in the vessel.

During these irradiations, gas bubbles were generated in the solution because of the radiolytic decomposition of water molecules in the solution. Multiple video cameras were used to record the behavior of bubble generation and transport in the solution. Seven six-channel thermocouples were used to record temperature gradients in the solution from self-heating. Measurements of hydrogen and oxygen concentrations in a helium sweep gas were recorded by a gas chromatograph to estimate production rates during irradiation. Full details of the Argonne Bubble Experiment are described in two earlier publications.[1,2] Figures 1 and 2 are schematics of the “Bubble-Experiment Apparatus.” Figure 3 is a photograph of the target vessel as set up. In this experiment, the electron beam of a linear accelerator was used to irradiate a typical solution volume to study (1) radiolytic bubble formation, size, and behavior and (2) thermal hydraulics.

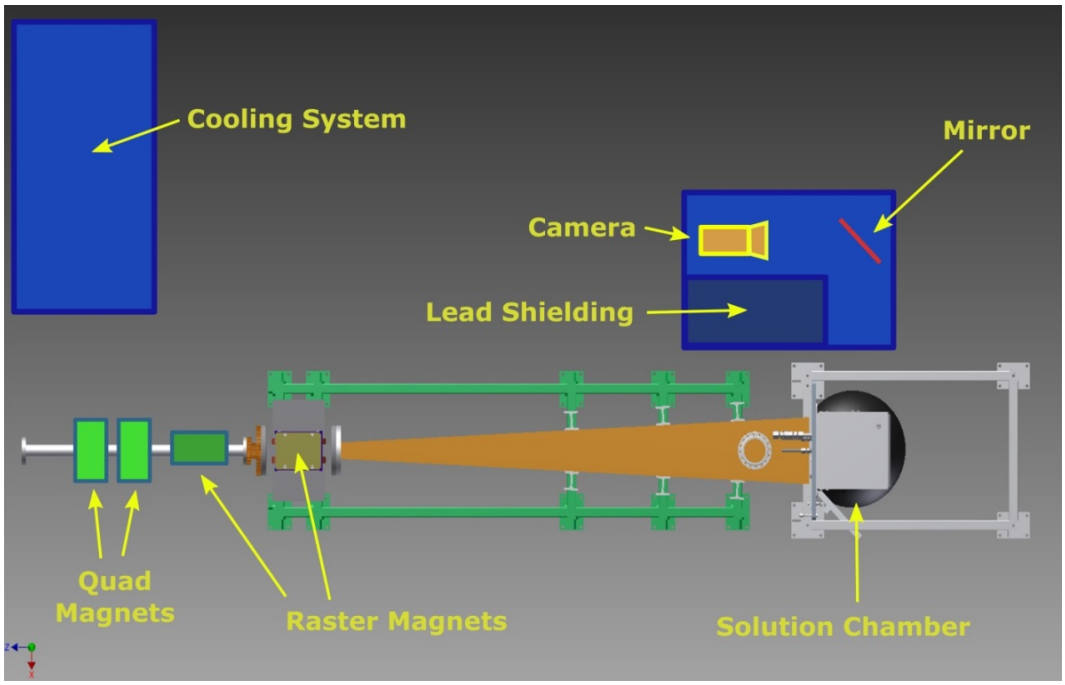

FIGURE 1 Major Elements of the Bubble-Experiment Apparatus

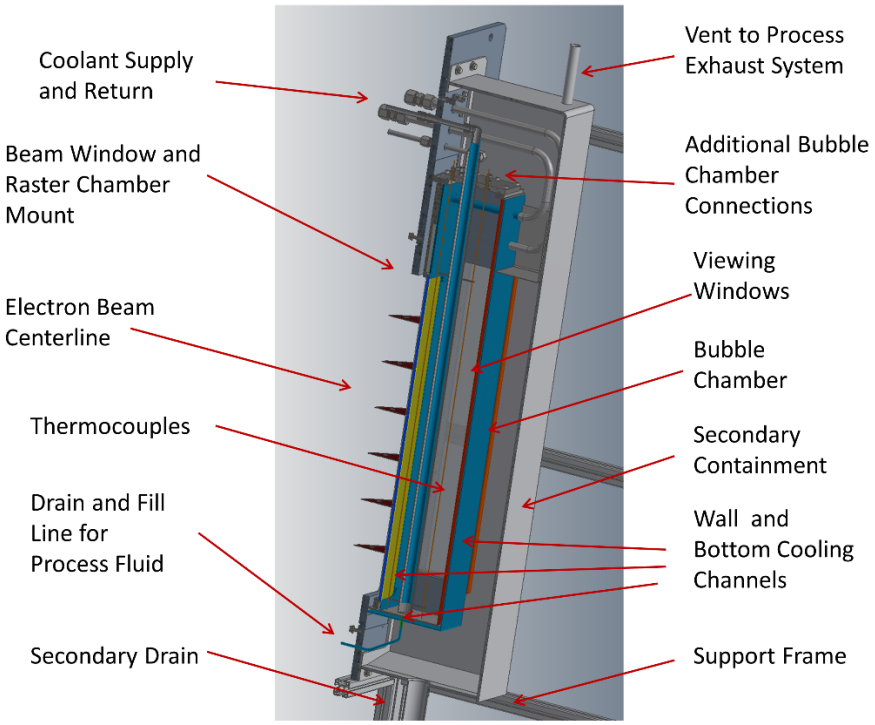

FIGURE 2 Schematic of the Bubble-Experiment Apparatus—Details of Irradiation Vessel

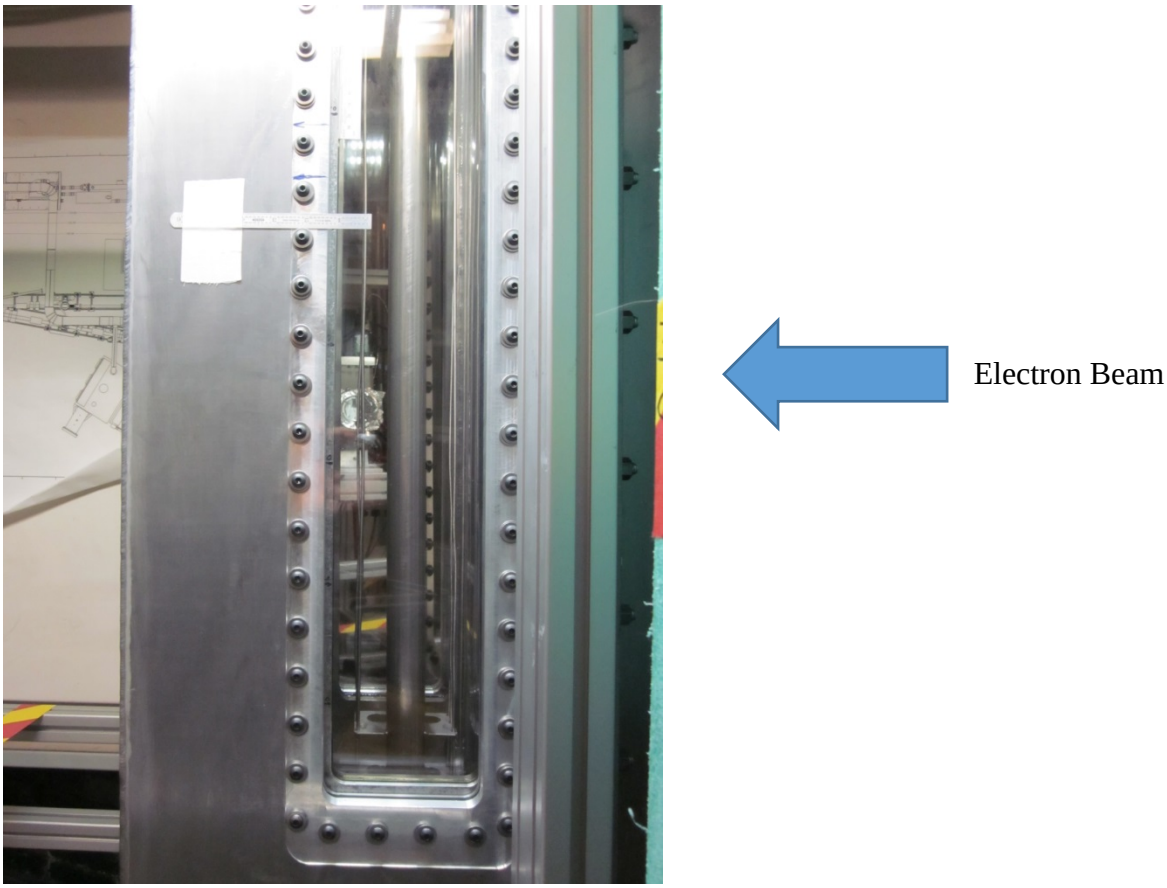

FIGURE 3 Photograph of the Assembled Bubble-Experiment Vessel

2 CFD METHODOLOGY

The CFD work in FY15 has consisted of the extension and refinement of techniques employed in the previous year.[1,2,3] Initially, two separate CFD codes, ANSYS CFX and OpenFOAM, were investigated in parallel in connection with the earlier preliminary efforts of FY14. The results from OpenFOAM, however, were found to provide greater fidelity with respect to experimental results and also allowed researchers to take advantage of all available computational resources without regard to software licensing limitations, and, therefore, all of the work presented in this report has arisen from its use. The custom hybrid Eulerian-Eulerian-Lagrangian solver that was developed using the OpenFOAM (version 2.3.x) toolkit consists of the addition of a Lagrangian phase (representing the radiolytically generated hydrogen and oxygen bubbles) on top of a pair of Eulerian phases (to account for the UO_2SO_4 solution and helium cover gas). The Eulerian-Eulerian phases are treated in a fully compressible manner, as it has been found that the temperature variations in the bubble chamber during irradiation are larger than is permissible for the use of the Boussinesq approximation that was employed in the past. Third-order polynomial expressions for the temperature-dependent properties of the uranyl sulfate solution have been used.[4] These expressions are included in Appendix A.1. A compressible large eddy simulation (LES) approach was found to be necessary to capture the heat transfer enhancement that arises from the natural convective flow in the laminar-turbulence transition regime observed under these conditions. As in the earlier work, the standard Smagorinsky sub-grid model was used herein.[5] The Lagrangian phase in the hybrid solver is coupled to the Eulerian phases by source terms that allow for two-way temperature and momentum transfer between the bubbles and the continuous phases.

The time-dependent, 3D simulations have been run on the simplified wetted-volume geometry shown in Figure 4. Extraneous geometric features (e.g., the thermocouple rods) that are not believed to have a large effect on the flow have been removed. In order to determine the grid independence of the numerical solution, multiple meshes were examined. The geometry was meshed using Cubit 14.0 (cubit.sandia.gov). Initial runs were performed on a coarse mesh with a base cell size of 5 mm (resulting in approx. 340,000 total hexahedral cells), followed by a fine mesh with a cell size of 2.5 mm (approx. 2.3 million hex cells total). Three levels of boundary layer cells were also included for all heat transfer surfaces. The surface mesh of the vessel's top wall is shown in Figure 5 for the fine-mesh case.

A representative 12 kW irradiation was simulated using a volumetric power deposition field calculated by MCNPX.[3] The incident beam profile used for the MCNPX simulations was taken from experimental measurements of the rastered beam. The resulting volumetric field was mapped into the CFD geometry as shown in Figure 6 and is assumed to be constant regardless of the presence of radiolytically generated bubbles. The 20 L uranyl sulfate liquid level is also shown in Figure 6 by the volume fraction contour representative of the free surface.

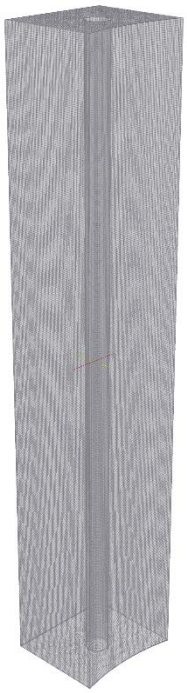

FIGURE 4 Bubble Chamber Geometry and Surface Mesh. The front curved surface is the location of the incident electron beam.

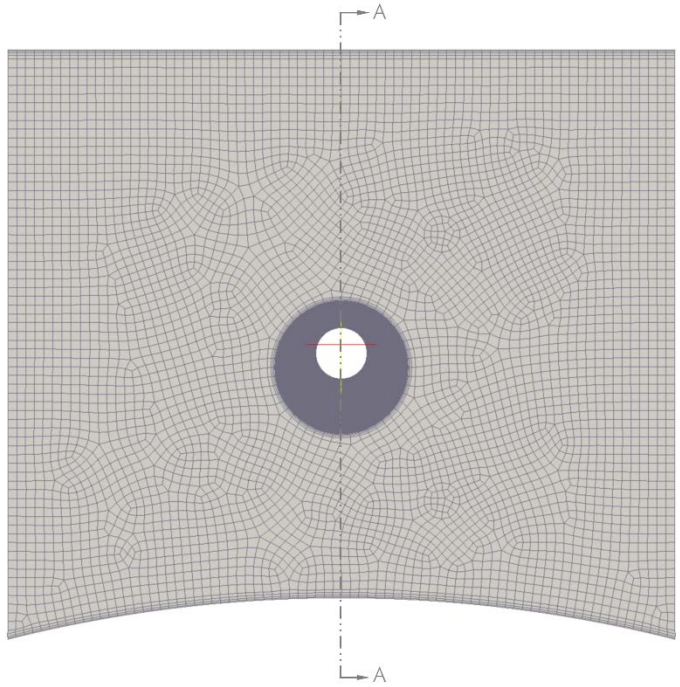

FIGURE 5 Detailed View of Surface Mesh on Top Surface for Fine Mesh (Base Cell Size 2.5 mm)

The side walls of the experimental vessel are assumed to be adiabatic, while the remaining walls are fixed at a specific temperature as controlled by the adjacent cooling channels. The representative fixed temperature was calculated to be 23.76 °C by adding the temperature rise from thermal resistances (e.g., from the thermal boundary layer in the cooling loop) to the experimentally measured coolant return temperature (20°C). The assumption of a uniform temperature is an approximation, as the coolant can be expected to become warmer as it exchanges heat with the bubble chamber along the coolant flow path, but the high flow rate of the coolant ensures that any downstream spatial variation is minimal for the case considered.

As homogeneous nucleation of bubbles was observed in experiments and the overall volume fraction of gas was found to be very low, the choice was made to treat the bubbles as spherical Lagrangian particles. The bubbles resulting from radiolysis were injected into the flow uniformly from a prescribed cell zone that was created at the lowest spatial extent of the rastered electron beam. The mean bubble diameter (267 μm) was measured from image analysis of high-speed video. Attempts were made to calculate the bubble generation rate from the radiolysis rate as measured in Van de Graff irradiations[6] combined with the measured bubble size from the actual experiment, but the results gave an unphysically high number of bubbles that was quite inconsistent with observations. Thus, a somewhat arbitrary injection rate of 10,000/s was

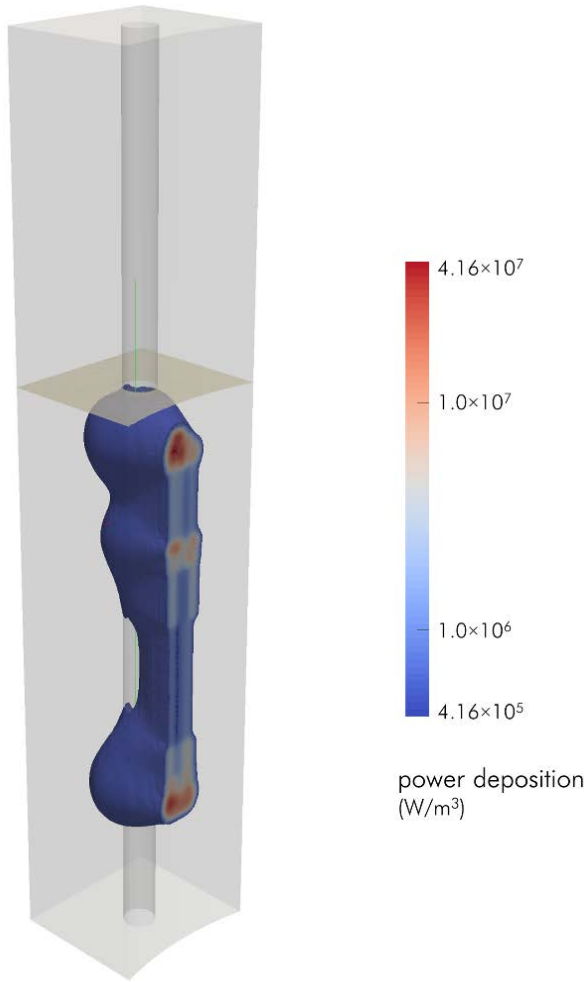

FIGURE 6 Volumetric Power Deposition Field from Incident Radiation (W/m^3) and Liquid Free Surface

selected on the basis of estimates taken from video of the experimental trial. Degassing of dissolved hydrogen directly from the top liquid surface (in lieu of forming bubbles) is one possible explanation for the disagreement between the observed bubble generation rate and the rate that would otherwise be expected. Alteration of the G-value in the current experiment as compared to the earlier work using Van de Graff irradiations offers another possible reason. On the basis of the results presented subsequently, it is not expected that the predictions will be appreciably sensitive to the bubble injection rate, but given the uncertainty concerning the bubble generation rate, future sensitivity studies should be conducted to establish this. It should be noted that the 10,000/s bubble generation rate is not a limitation of the OpenFOAM solver; the solver itself is capable of arbitrarily large injection rates.

3 CFD RESULTS

The CFD cases were run on a high-performance computing cluster and generally required several days to complete when performed on 100s of cores. This is because a transient heat-up period of more than 1000 seconds was required. A typical result is shown in Figure 7, where the instantaneous positions of the radiolytically generated bubbles have been indicated. The individual bubbles are colored by their temperature as they rise through the uranyl sulfate solution. The typical rise time for the bubbles to reach the free surface was approximately 10 seconds.

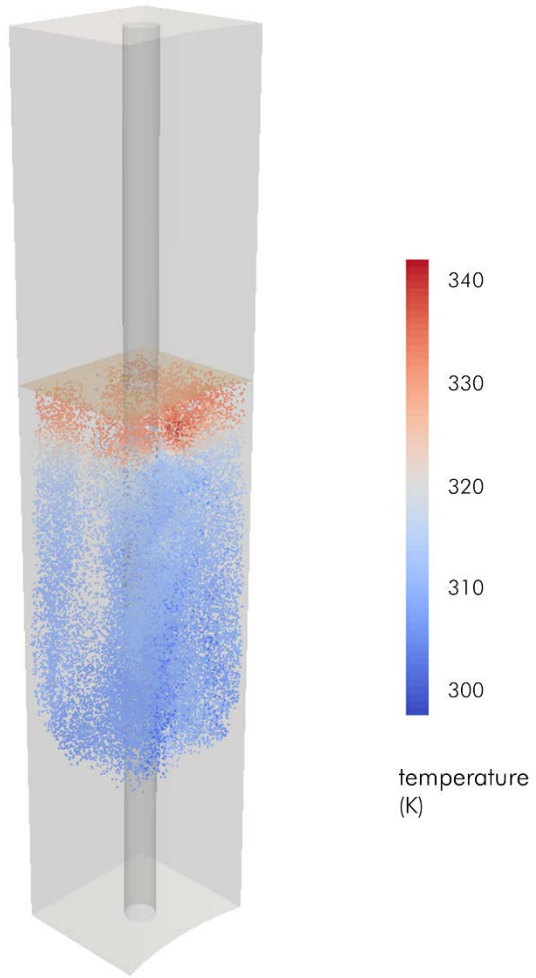

FIGURE 7 Positions of Radiolytically Generated Bubbles in the Uranyl Sulfate Solution. Bubbles are colored by their instantaneous temperature.

Contour plots along Section A-A (indicated in Figure 5) have been included to demonstrate the prevailing features of the flow. Figure 8(a) shows contours of the time-averaged velocity in the z-direction (i.e., the upward velocity). Two strong natural-circulation loops clearly exist in the front of the bubble chamber (i.e., the half nearest to the incident beam). Sustained downward flow exists at both the front cooling wall and the wall of the central cooling channel, with a fast upward plume in between. In the rear half of the chamber (i.e., the half away from the incident beam), a similar situation exists, with downward flow at the walls, but the upward plume is much less pronounced—the frontal plume has a time-averaged maximum upward velocity of 5.21 cm/s compared to 0.11 cm/s for the plume in the rear of the vessel. This occurs because much of the upward flow from the frontal plume is transferred rearward for its downward transit. Fluid is then re-entrained forward near the bottom of the chamber.

Contours of the upward velocity at an instantaneous point in time are shown in Figure 8(b). Eddies are clearly visible as the strength of the frontal plume induces turbulence in the fluid. This turbulence, in turn, greatly increases heat transfer by increasing the effective thermal conductivity. The frontal plume exists primarily in the region above where the rastered electron beam is incident, leaving the fluid below relatively quiescent except for small secondary vortices at the bottom of the chamber.

The volumetric temperature field along with velocity vectors are shown in Figures 9(a) and 9(b), respectively. The temperature field can be seen to vary strongly as a function of the depth below the liquid surface. However, in the lateral directions, the temperature distribution is surprisingly uniform, given that the majority of the incident radiation is absorbed only in the front side of the chamber. Ultimately, though, both turbulence and the large convective exchange that occurs between front and back are able to maintain uniformity.

3.1 EFFECT OF BUBBLES

The effect of the bubble generation on the predicted thermal hydraulic behavior was examined by running cases with and without bubble generation included. The results showed minimal differences regardless of the presence of the radiolytically generated bubbles. The reason for this small change is that, even given the large generation rate of bubbles (10,000 bubbles/s), the volume fraction of the gas bubbles is always well below 1% because of their small size. Therefore, the presence of this small amount of gas is never able to heavily reduce the effective thermal conductivity of the solution or to greatly affect the convective behavior.

For example, for the 12 kW irradiation, the small alteration to the time-averaged upward velocity profile caused by the bubbles is shown in Figure 10. The velocity is plotted along the indicated line in the region where the upward plume is the strongest (35.4 cm below the free surface). The plume in the front of the irradiated vessel is augmented slightly by the rising bubbles—the peak velocity is 5.21 cm/s as compared to 5.03 cm/s without bubble generation. However, this modification to velocity field was found to alter the heat transfer performance in only a limited fashion; the presence of bubbles was predicted to cause less than 0.1ºC reduction in the mean temperature of the solution. While the effect is exceedingly small, it is thus seen that

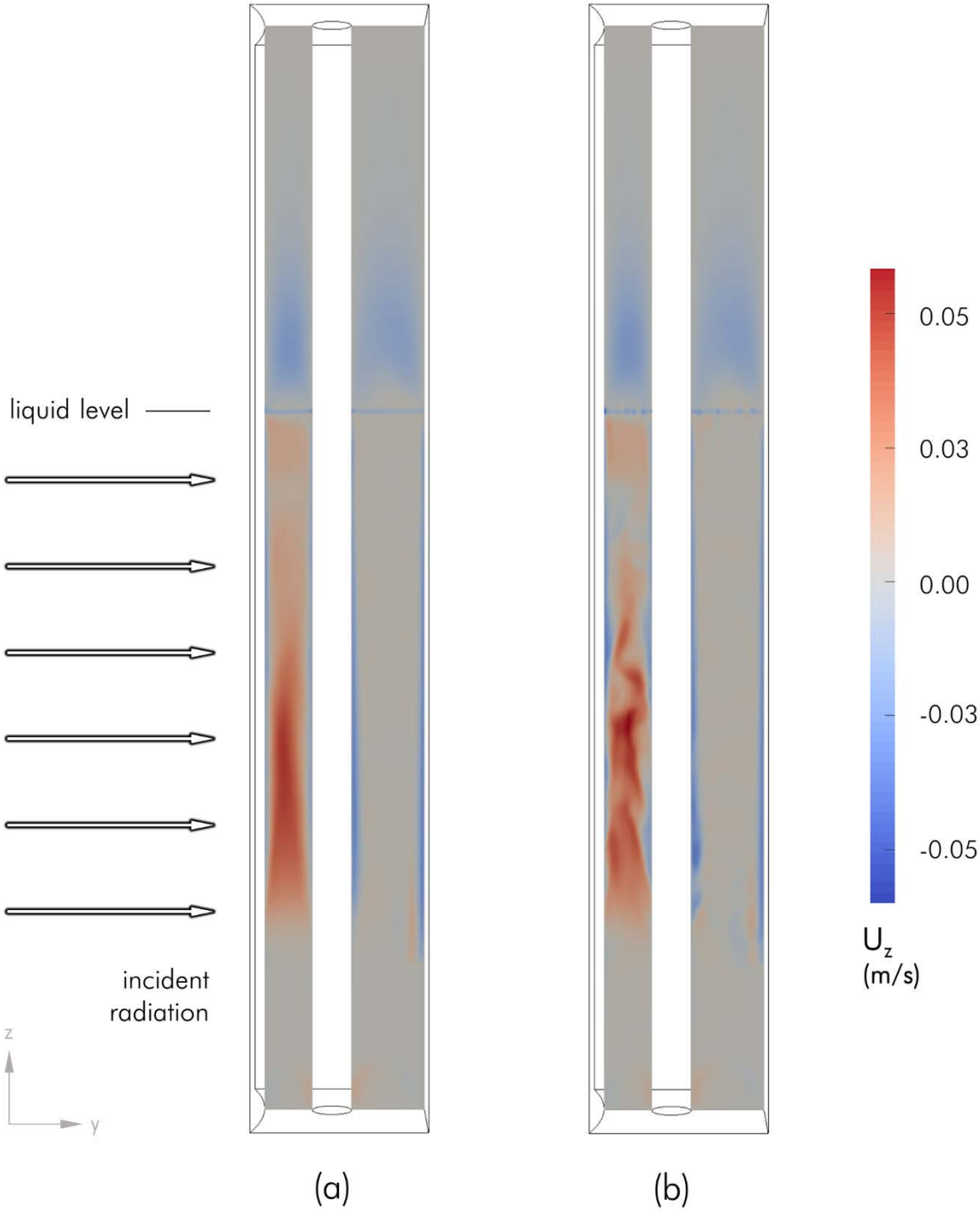

FIGURE 8 (a) Time-Averaged Upward Velocity Contours (U_z) with Indicated Liquid Level; (b) Instantaneous Upward Velocity Contours (U_z) with Indicated Liquid Level

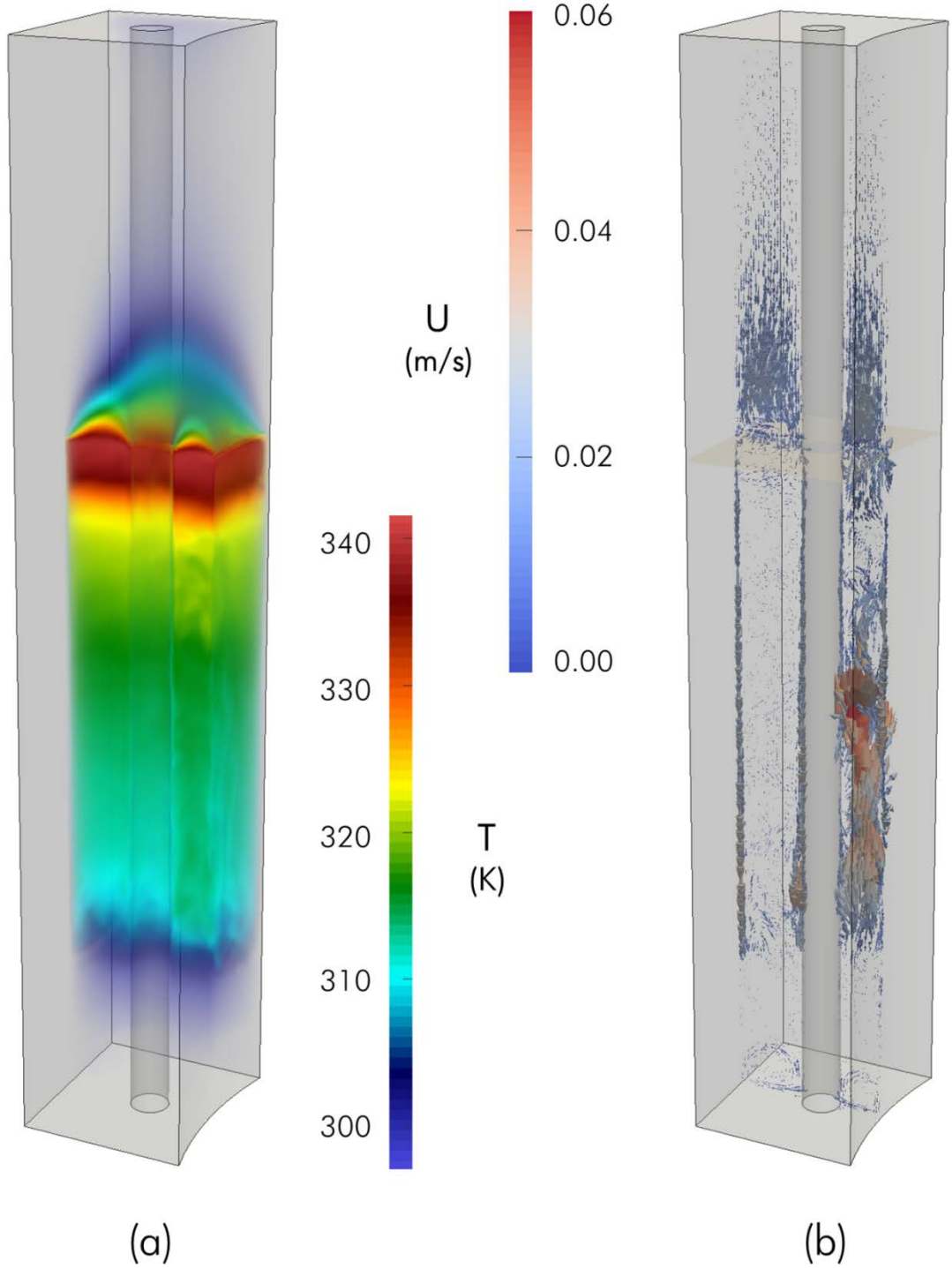

FIGURE 9 (a) Instantaneous Temperature Field; (b) Instantaneous Velocity Vectors Colored by Velocity Magnitude

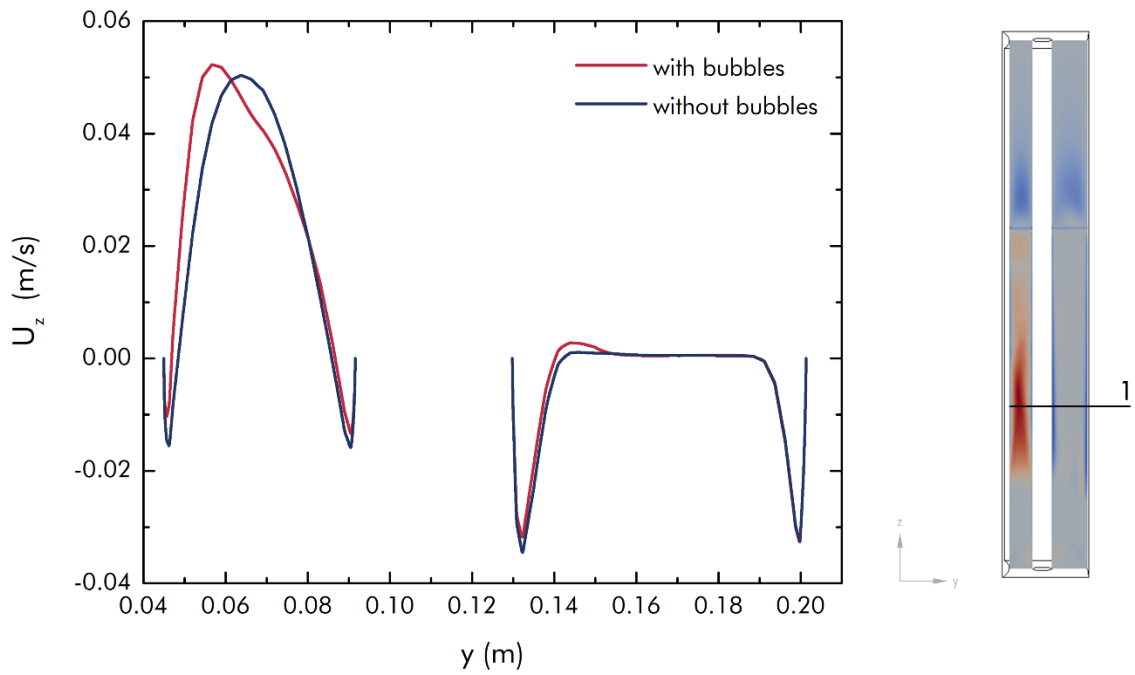

FIGURE 10 Upward Velocity Profile across the Indicated Line (1) with and without Bubble Generation

the addition of the bubbles actually leads toward a decrease in mean solution temperature due to increased circulation velocity rather than an increased temperature due to any diminishing of the effective thermal conductivity of the solution. As noted above, sensitivity studies to explore the influence of the bubble injection rate could be conducted in the future to provide further confidence in this observation.

3.2 COMPARISON TO THERMOCOUPLE MEASUREMENTS

A quantitative comparison of CFD and experimental results was made by comparing thermocouple data from the 12 kW irradiation to the predicted temperature field at collocated points in the simulation. In the experimental setup, 42 total thermocouples were arranged around the central cooling channel at the seven positions in the x-y plane shown in Figure 11, labeled TC1 through TC7. At each of the seven positions, a stainless steel mounting rod was used to hold the individual thermocouples at one of six equally spaced depths in the z-direction. For the 20 L uranyl sulfate fill level, the resulting distance below the initial liquid surface for each of these depths is as shown in Table 1. The negative distance for the sixth depth position indicates it is in the gas head space above the liquid surface. The large array of thermocouples allows for thorough discernment of the spatial variation of the temperature field and for the estimation of the average temperature of the irradiated solution.

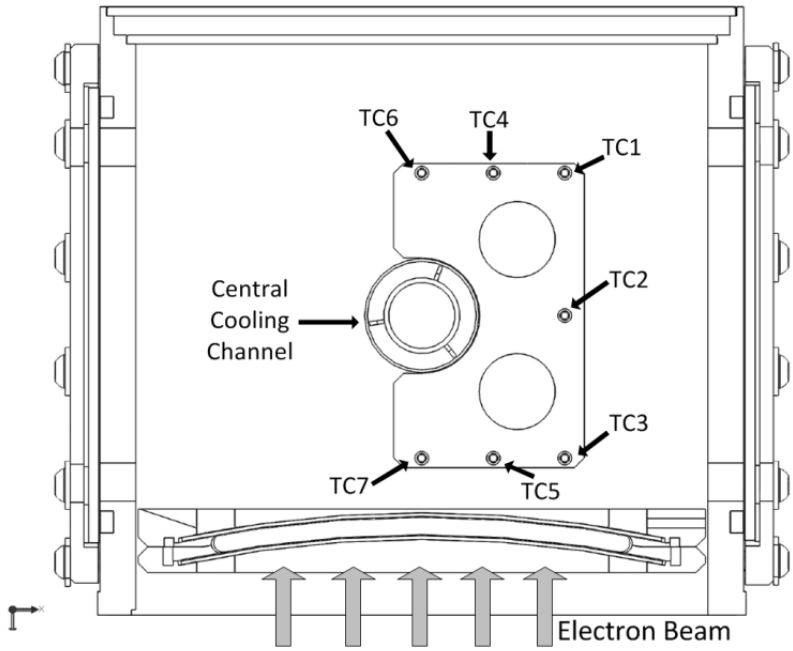

FIGURE 11 Cross Section of the Experimental Primary Containment Vessel (Figure Taken from Reference 3)

TABLE 1 Depth of Thermocouple Channels beneath the Liquid Surface for 20 L Fill Level

Depth	Distance below free surface (cm)
1	54.5
2	37.0
3	29.1
4	16.4
5	3.7
6	-11.5

Much like the CFD results, the experimental data showed the temperature field to be largely uniform at any given depth, with large spatial variations in the x-y plane existing only due to direct incidence of the electron beam on the frontmost thermocouples (see, for example, the experimental data for TC5 and TC7 in ref. 3). Therefore, the area-weighted average temperature across a given depth has been adopted as the most suitable metric for comparison of the experiments to CFD. The averaging procedure was performed as in the work of Chemerisov et al.[3] Thermocouple channels that were clearly adversely affected by internal heating from irradiation (TC5-2, TC5-3, TC5-4, TC7-2, TC7-3, and TC7-4) were not included in the averaging. These thermocouples, which were at the front of the experimental vessel, were each at

least 25ºC hotter than the other thermocouples at the same depth and clearly showed indications of dysfunction.

A comparison of experimental and CFD results is shown in Figure 12. The steady-state temperature at the bottom of the bubble chamber (Depth 1) is low and then rises to a maximum at the uppermost extent of the liquid (Depth 5). The temperature then drops within the gas headspace (Depth 6) where the cover gas circulates. The RMS error between the experimental data and CFD predictions across all thermocouple measurements is 10.4°C. The vast majority of this error occurs at the mid-depths within the uranyl sulfate solution (specifically, Depths 2, 3, and 4), where the thermocouple readings from experiments are generally more than 15 C higher than the predictions from CFD.

Some of this disagreement appears to arise from an inconsistency in the power deposition field that is mapped into the CFD geometry. In the simulation, this field is concentrated most heavily at Depth 5; however, the experimental data (e.g., Figure 10(g) in ref. 3) instead clearly indicate that the greatest beam incidence should occur at Depths 2, 3, and 4 (with thermocouples at the other depths largely unaffected). Therefore, it is not surprising that the computationally predicted temperatures at mid-depths are low, as a large fraction of the power deposition is erroneously applied to the fluid at higher depths, where it has far less effect on the temperature field below.

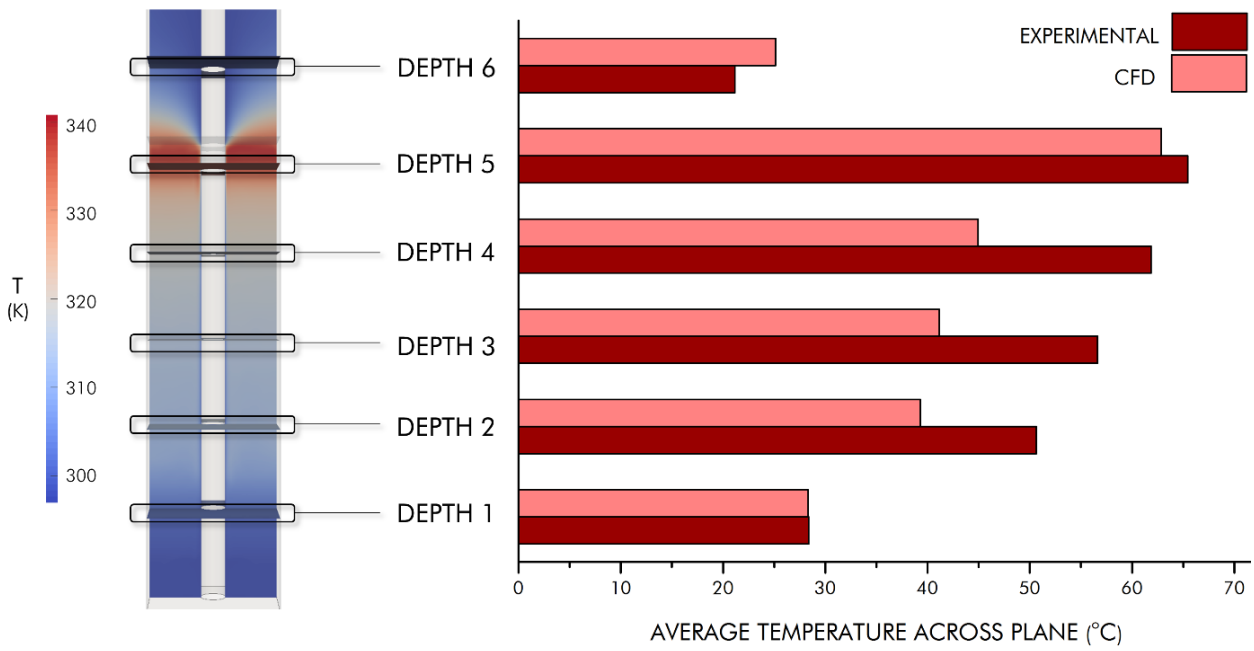

FIGURE 12 Area-Weighted Average Steady-State Temperature for a Given Depth from Experiments and from Numerical Simulations

An additional source of the disagreement between the CFD and experimental data at middle depths can arise from internal heating of the thermocouples, as this is the region of incidence for the rastered electron beam. In order to examine the issue of direct thermocouple heating by the beam, an estimate of the fluid/thermocouple temperature difference for nominal conditions at Depth 3 was sought. Full details of these CFD calculations are included in Appendix A.2. The results indicated that a thermocouple struck by the beam would have a temperature 15°C higher than the surrounding fluid. Therefore, it is a reasonable assumption that the discrepancies between the numerical results and the experiment are at least partially due to internal heating of the thermocouple from the beam impingement.

Predictions for the uppermost and lowermost thermocouple data in the liquid, however, are very good. For example, the steady-state temperature averaged across Depth 5 (just below the liquid surface) is predicted by CFD to be 62.9 °C, as compared to the experimental value of 65.4 °C. The fidelity of this prediction is very important because cooling system design must be tailored to the prevention of boiling in the solution. Therefore, correct prediction of the maximum temperature in the liquid is essential and has been achieved by the developed CFD methodology.

3.3 COMPARISON TO VELOCITY MEASUREMENTS

Further quantitative comparisons with experimental data could be made using bubble velocity estimates that resulted from analysis of high-speed video images. By comparing the experimental values with those predicted by CFD, the quality of the coupled Lagrangian bubble cloud evolution scheme could be determined. The images were taken in the interrogation regions shown in Figure 13. Similarly sized regions were demarcated in the CFD mesh, and the bubble cloud was parsed to extract the average velocity of all of the particles existing within those regions.

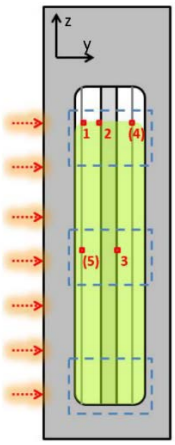

FIGURE 13 High-Speed Imaging Locations (Positions 1 and 2) Used for Determination of Bubble Velocities (Figure Taken from Ref. 3)

A comparison of the CFD and experimental results is shown in Table 2. The velocity at position 2 was reasonably well predicted, with the upward bubble velocity (U_z) falling within the bounds of the experimental error and the predicted lateral velocity (U_y) falling just below the experimental bounds. The velocity components at Position 1, however, were not predicted well, with both values falling outside of the range of experimental uncertainty. There are several possible causes of this disagreement. Some of the error is likely due to uncertainty in the exact position of the depth of field of images taken from high-speed photography. The numerical treatment of the gas-liquid interface is also a potential source of error, as the imaging locations are very near the surface and are therefore in regions where parasitic velocities could exist. In order to investigate this discrepancy between experiments and simulations, alternative interfacial treatments and sub-grid-scale turbulence models can be investigated to determine the sensitivity of the sub-surface velocities.

TABLE 2 Predicted and Experimentally Estimated Bubble Velocities (Positions and Directions Are Shown in Figure 13)

	U_z (cm/s)		U_y (cm/s)	
Position	Experimental	CFD	Experimental	CFD
1	4.0 ± 1.2	5.7	1.0 ± 0.3	-0.2
2	4.9 ± 1.0	4.9	0.8 ± 0.2	0.4

3.4 EFFECT OF CENTRAL COOLING CHANNEL

After achieving a satisfactory match to the existing experimental trials, alternative design concepts could be examined without the costly fabrication of new experimental hardware. One design alteration that was examined was removal of the central cooling channel. While the removal of the channel would reduce the surface area of the cooled wall in contact with the fluid, it was thought that the resulting improvement to the natural convection loop could potentially lower temperatures in the vessel (as the density-driven circulation would be less impeded).

Using the CFD modeling approach that has been developed, a case was therefore run with the central cooling channel taken out. While the plume in the front of the vessel was predicted to have a larger spatial extent, its upward velocity was found to be slower (3.82 cm/s compared to 5.21 cm/s originally). Turbulent mixing in the front of the vessel was also found to be attenuated. The average temperature of the solution was therefore calculated to be 320.0 K, compared to 312.8 K for the case with the cooling channel present. Thus, in this case, the design modification has been found to be unfavorable and will not be pursued experimentally.

4 CONCLUSION

The developed CFD methodology based on the open-source CFD toolkit OpenFOAM has proven capable of providing good predictions of the thermal hydraulic behavior within the accelerator-irradiated uranyl sulfate solution reactor experiments. The most critical quantity of interest, the maximum liquid temperature within the vessel, was predicted to within 4% of the experimental value. For the simulated conditions of the bubble chamber experiment, the effect of the radiolytically generated bubbles on overall heat transfer and flow patterns of the solution was found to be minimal. Additional studies and simulations could be readily performed to determine if this conclusion also holds true for the full-scale solution assembly. A key advantage of the method employed here is that it is easily extended to larger geometries and more computational processors without software licensing limitations, thus enabling high-fidelity LES simulations of the multiphase thermal hydraulic phenomena encountered to be conducted for the complete solution vessel as warranted.

5 ACKNOWLEDGMENTS

The computational resources of the Falcon supercomputing cluster at INL's High Performance Computing Center are gratefully acknowledged. This work was funded by the Department of Energy Office of Nuclear Non-Proliferation.

6 REFERENCES

1. Chemerisov, S., R. Gromov, V. Makarashvili, T. Heltemes, Z. Sun, K. Wardle, J. Bailey, K. Quigley, D. Stepinski, and G. Vandegrift, Design and Construction of Experiment for Direct Electron Irradiation of a Uranyl Sulfate Solution: Bubble Formation and Thermal Hydraulics Studies, ANL/CSE-14/29, Argonne National Laboratory, October 2014, in press.

2. Chemerisov, S., R. Gromov, V. Makarashvili, T. Heltemes, Z. Sun, K. Wardle, J. Bailey, and G. Vandegrift, "Experimental Setup for Direct Electron Irradiation of the Uranyl Sulfate Solution: Bubble Formation and Thermal Hydraulics Studies", Proceedings of the Mo-99 2014 Topical Meeting on Molybdenum-99 Technological Development, June 24-27, 2014, http://mo99.ne.anl.gov/2014/pdfs/papers/S9P10%20Paper%20Chemersiov.pdf

3. Chemerisov, S., R. Gromov, V. Makarashvili, T. Heltemes, Z. Sun, K. Wardle, J. Bailey, K. Quigley, D. Stepinski, J. Jerden, M. Basavarajappa and G. Vandergrift, "Generation of Gas Bubbles in a Fissioning Uranyl Sulfate Solution Using an Electron Beam Linac," Proceedings of the Mo-99 2015 Topical Meeting on Molybdenum-99 Technological Development, August 31-September 3, 2015, http://mo99.ne.anl.gov/2015/pdfs/papers/S9P9_Paper_Heltemes.pdf

4. Youker, A., D.C. Stepinski, L. Ling, and G.F. Vandegrift, Mo Recovery and Physical Properties of Uranyl Sulfate Solutions, ANL/CSE-13/20 REV 1, Argonne National Laboratory, October 2014, http://www.ipd.anl.gov/anlpubs/2014/11/109440.pdf.

5. Pope, S., Turbulent Flows, Cambridge University Press, 2000.

6. Sun, Z., K. Wardle, K. Quigley, R. Gromov, A. Youker, V. Makarashvili, J. Bailey, D. Stepinski, S. Chemerisov, and G.F. Vandegrift, Micro-Bubble Experiments at the Van de Graff Accelerator, ANL/NE-15/2, Argonne National Laboratory, October 2014, http://www.ipd.anl.gov/anlpubs/2015/05/113420.pdf.

APPENDIX A.1:

THERMOPHYSICAL PROPERTIES OF URANYL SULFATE SOLUTION

This page intentionally left blank

APPENDIX A.1:

THERMOPHYSICAL PROPERTIES OF URANYL SULFATE SOLUTION

The third-order polynomials used to determine the thermophysical properties of the 140 g/L uranyl sulfate solution were created from fits to the data in ref. 4. The resulting expressions are as follows (with *T* in units of K):

$$\kappa = -31.171 + 2.842 \times 10^{-1}\, T - 8.493 \times 10^{-4}\, T^2 + 8.475 \times 10^{-7}\, T^3 \quad W/m \cdot K$$

$$\mu = 0.216 - 1.889 \times 10^{-3}\, T + 5.538 \times 10^{-6}\, T^2 - 5.435 \times 10^{-9}\, T^3 \quad Pa \cdot s$$

$$C_p = 3335 \quad J/kg \cdot K$$

$$\rho = 1053.3 + 1.3699\, T - 2.976 \times 10^{-3}\, T^2 \quad kg/m^3$$

This page intentionally left blank

APPENDIX A.2:

CFD CALCULATIONS OF THERMOCOUPLE INTERNAL HEATING

This page intentionally left blank

APPENDIX A.2:

CFD CALCULATIONS OF THERMOCOUPLE INTERNAL HEATING

A CFD analysis was performed to estimate the effect of the internal heating of the thermocouple on the temperature measurements. The averaged thermocouple measurement at thermocouple channel Depth 3 as shown in Figure 12 was evaluated. At this depth, the numerical steady-state temperature of the fluid was 43°C and the experimental measurement was 57°C, a discrepancy of 14°C.

A single average thermocouple at Depth 3 was modeled. The thermocouple was located in the center of a stream tube approximately 5 cm in diameter. The CFD modeling considered two convective cooling mechanisms at the thermocouple surface. The first was the natural convection of the fluid due to the temperature difference between the fluid and thermocouple surface. The second was considered as forced convection due to the general circulation in the bubble chamber. On the basis of the numerical results shown in Figure 8(b), the average velocity along the thermocouples at Depth 3 was estimated to be 0.015 m/s. This value was introduced into the CFD model as a forced flow along the thermocouple in the upward vertical direction. The internal heat generation within the thermocouple model was assumed to be uniform in both the axial and radial directions. The magnitude of the heat generation density was estimated by increasing the heat generation in the fluid at Depth 3 by the ratio of the densities of the fluid to the average density of the thermocouple material. Also, the material properties of the thermocouple were considered uniform with averaged values. These simplifying assumptions are justified because of the geometry of the thermocouple. The small diameter of the thermocouple compared to its length results in a small characteristic length in the radial direction and a large characteristic length in the axial direction that in turns allows for assuming negligible thermal resistance in the radial direction and negligible thermal conductivity in the axial direction. Hence, the thermal behavior at any thermocouple junction location is essentially a local phenomenon.

The model and results of this CFD analysis are shown in Figure A-2.1. The flow was introduced at the bottom of the stream tube at a uniform velocity and a temperature of 43°C. This inlet location corresponds to the bottom of the bubble chamber and the fluid inlet temperature is obtained from the temperature of the fluid as calculated and indicated in Figures 9(a) and 12, Depth 3. The results of this analysis under the above assumed conditions indicate that the thermocouple will have a temperature of approximately 58°C, which is in good agreement with the experimental measurements shown in Figure 12 at the Depth 3 location. Therefore, the assumption that the discrepancies between the numerical results and the experiment are due to internal heating of the thermocouple from the beam impingement is reasonable.

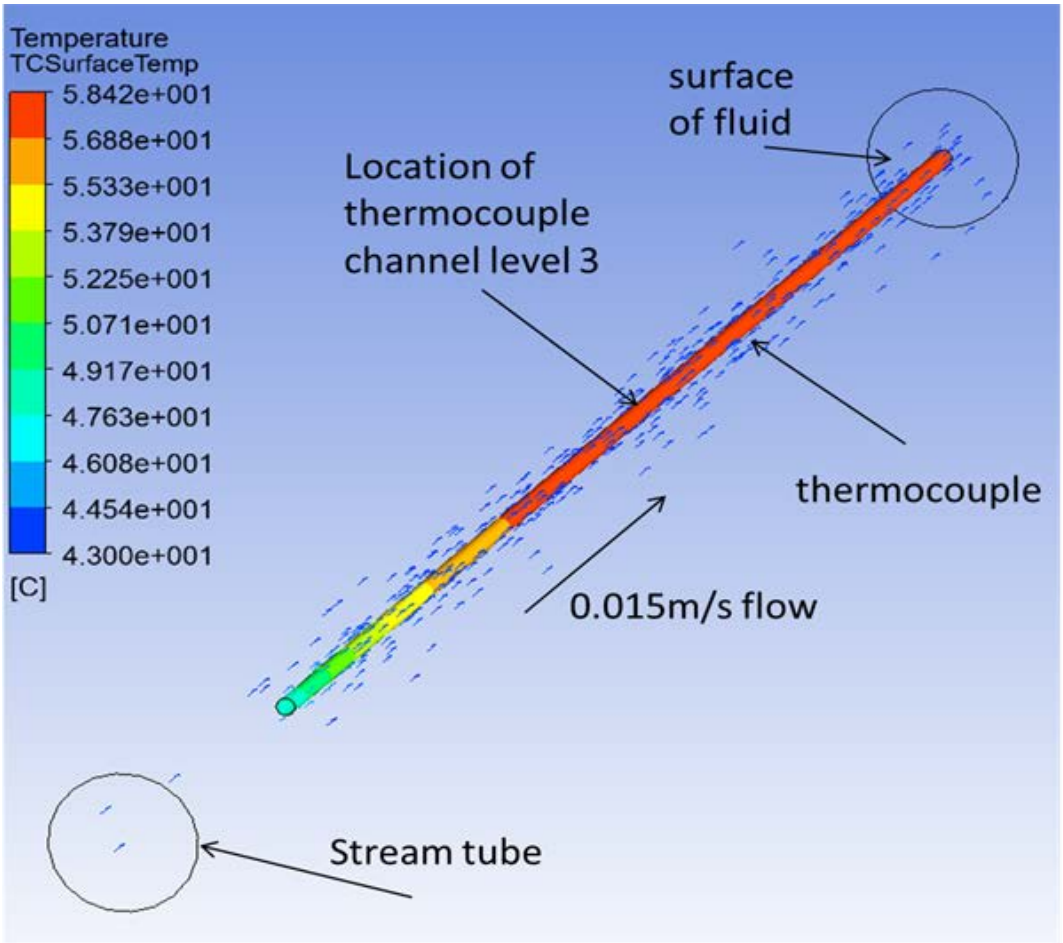

FIGURE A.2.1 CFD Results for Internal Heating of the Thermocouples

Nuclear Engineering Division
Argonne National Laboratory
9700 South Cass Avenue, Bldg. 208
Argonne, IL 60439-4854

www.anl.gov

Argonne National Laboratory is a U.S. Department of Energy
laboratory managed by UChicago Argonne, LLC